Noname manuscript No.
(will be inserted by the editor)

Advanced Tsunami Numerical Simulations of The Puerto Rico October 11, 1918 Mona Passage Tsunami

Alberto M. López-Venegas · Juan Horrillo · Victor Huérfano · Aurelio Mercado · Alyssa Pampell-Manis

Received: date / Accepted: date

Abstract The most recent tsunami observed along the coast of the island of Puerto Rico occurred on October 11, 1918 after a magnitude 7.2 earthquake was generated in the Mona Passage. The earthquake was responsible for triggering a tsunami that mostly affected the northwestern coast of the island of Puerto Rico. Runup values from a post-tsunami survey indicated the waves reached up to 6 meters. A controversy regarding the source of the tsunami has resulted in several numerical simulations involving either fault rupture or a submarine landslide as the most probable cause of the tsunami. Here we follow up on previous simulations of the tsunami from a submarine landslide source off the western coast of Puerto Rico as triggered by the earthquake. Improvements from our previous study include: (1) a higher resolution bathymetry, (2) a 3D-2D coupled numerical model specifically developed for the tsunami event, (3) the use of the non-hydrostatic numerical model NEOWAVE, featuring two-way nesting capabilities, and (4) a comprehensive energy analysis to determine the time of full tsunami wave development. The three-dimensional Navier-Stokes model TSUNAMI3D for two fluids (water and landslide) is used to determine the initial wave characteristic generated by the submarine landslide. Employing NEOWAVE allows us to solve for coastal inundation, wave propagation and detailed runup. Our results are in agreement with previous works in which a submarine landslide is favored as the most probable source of the tsunami, and the improvement in the resolution of the bathymetry yield inundation of the coastal areas that compare well to values from a post-tsunami survey. Our unique energy analysis indicates that the majority of wave energy is isolated to the wave generation region, particularly at depth near the landslide, and once the initial wave propagates away from the generation region its energy begins to stabilize.

Keywords 1918 Mona, tsunami, submarine landslide, Volume of Fluid, three dimensional model, non-hydrostatic model

Received: date / Revised version: date

Alberto M. López-Venegas
Department of Geology University of Puerto Rico - Mayag¨uez Campus, Mayagüez, PR.

Juan Horrillo
Texas A&M University at Galveston, Galveston, TX.

Victor Huérfano
Puerto Rico Seismic Network, University of Puerto Rico - Mayag¨uez Campus, Mayagüez, PR.

Aurelio Mercado
Department of Marine Sciences University of Puerto Rico - Mayag¨uez Campus, Mayagüez, PR

Alyssa Pampell-Manis
Texas A&M University at Galveston, Galveston, TX.

Introduction

The most recent tsunami affecting the island of Puerto Rico in the northeastern Caribbean occurred on October 11, 1918. The tsunami, which affected mostly the northwest coast of the island, was observed shortly after a $M_w 7.2$ (Doser et al., 2005) earthquake originating somewhere in the Mona Passage (Figure 1). A post-tsunami survey carried out by Reid and Taber (1919) reported runups ranging from 3 to 8 m along the northwest coast of Puerto Rico, approximately four million dollars in damage, and 110 casualties from the earthquake destruction and 40 people drowned as a result of the tsunami. The first effort in modeling the October 11, 1918 tsunami came from Mercado and McCann (1998), who assumed an instantaneous co-seismic dislocation as the initial tsunami source. Although their fault model yielded overall good agreement, it was unable to reproduce the observed negative polarity of the first wave arrival and detailed runups. An alternative mechanism for this tsunami event is based on

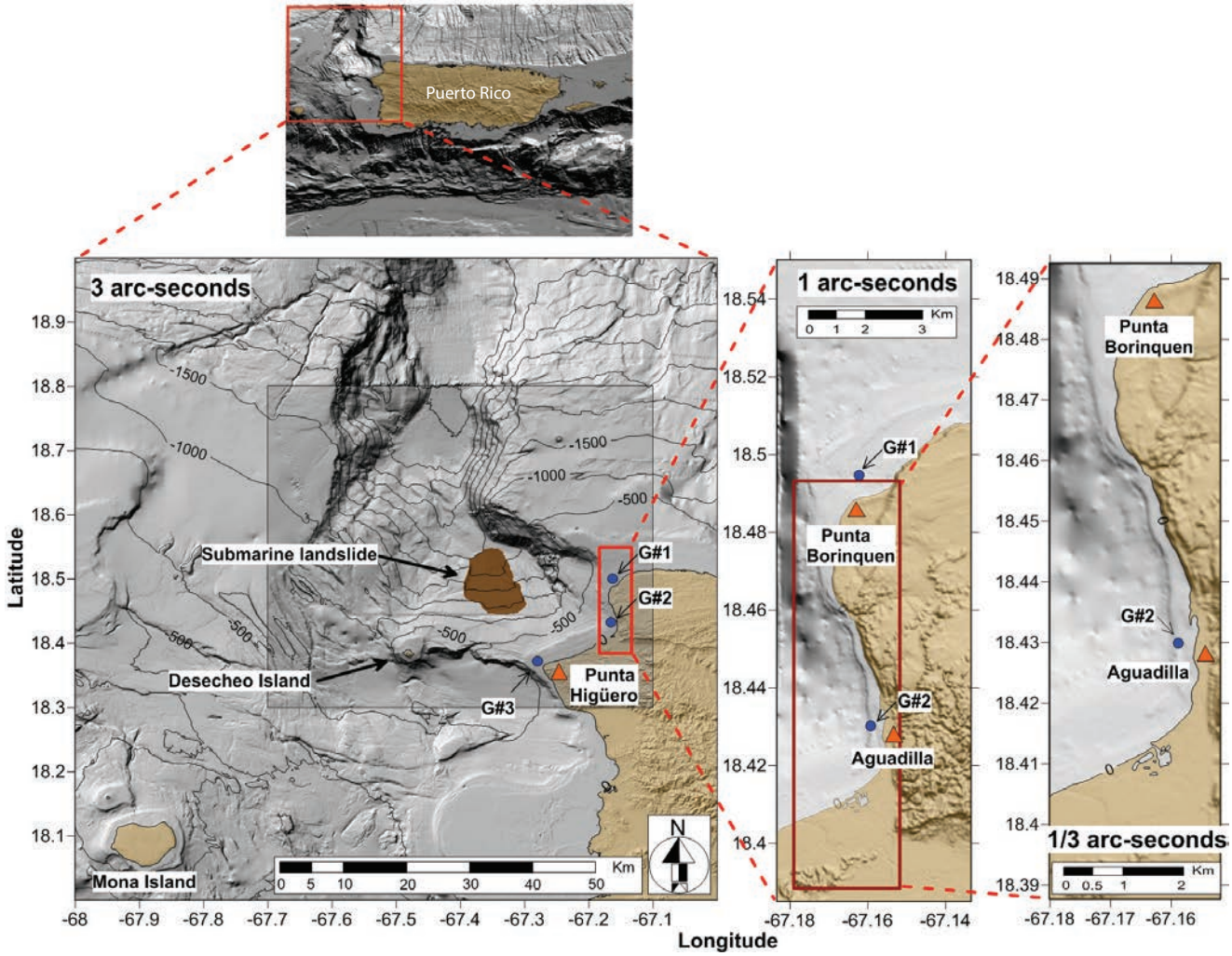

Fig. 1 Bathymetry near Puerto Rico's northwest corner (Mona Passage) and nested domains (3, 1, and $1/3$ arc-seconds of resolution) used by the 2D non-hydrostatic numerical model NEOWAVE for the calculation of the tsunami wave propagations and runup. The generation domain (gray shadow area on the 3arc-seconds domain) is used by the 3D numerical model TSUNAMI3D for the calculation of initial tsunami waves generated by the submarine landslide.

the assumption that the earthquake triggered a submarine landslide. Great debate over the two sources of the tsunami existed until high resolution bathymetry and multi-channel seismic studies were collected by the US Geological Survey (USGS) during the first decade of the 21^{st} century (ten Brink et al., 2004; Chaytor and ten Brink, 2007, 2010) that showed evidence of a submarine landslide. López-Venegas et al. (2008) used the identified geometry of the landslide, excavation area, and seismic reflection profiles to suggest the landslide as the most probable generation mechanism for the tsunami, and ran simulations using the identified parameters to compare arrival times, polarity of leading wave, and wave amplitudes close to the shore where runup values were measured by the post-tsunami survey of Reid and Taber (1919). In addition to the good agreement provided by the modeling, López-Venegas et al. (2008) favored the landslide over the dislocation model because historical evidence indicated two telegraph cables failed in the landslide generation area (Reid and Taber, 1919) and no clear evidence of recent faulting or seafloor rupture was evident in either the seismic profiles or the multi-beam bathymetry, respectively. Attempts to uncover the possibility that a submarine slide was the major contributor of the tsunami waves has been widely documented in the literature, for example Hornbarch et al. (2008). Their analysis suggested that a submarine slide was also a plausible alternative explanation for the generation of the 1918 tsunami.

Recent assessments of tsunami hazards along the Puerto Rico coastal regions carried out by the USGS have identified several large tsunamigenic submarine landslide scarps (ten Brink et al., 1999, 2004). The study identified the presence of large scarps carved out on the northern margin of the Puerto Rico-Virgin Islands carbonate platform. The scarps show evidence that the northern slope of Puerto Rico has

undergone massive submarine slope failures. As a consequence, massive underwater landslides in the vicinity of the Puerto Rico Trench are considered a potential hazard (see also Dunbar and Weaver, 2008) and the effects of such an event on the coastal region require further analysis using state of the art numerical modeling tools. Thus, this study intends to re-assess the 1918 Mona tsunami by using a 3D-2D coupled numerical model which has its origin from two existing tsunami numerical models: TSUNAMI3D (Tsunami Solution Using Navier-Stokes Algorithm with Multiple Interfaces) (Horrillo, 2006; Horrillo et al., 2013) and NEOWAVE (Non-hydrostatic Evolution of Ocean WAVE) (Yamazaki et al., 2008).

In the area of the landslide generation, the initial tsunami source is determined by the 3D Navier-Stokes (NS) model, TSUNAMI3D, developed by the University of Alaska Fairbanks (UAF) and Texas A&M University at Galveston (TAMUG). The tsunami wave propagation and the detailed inundation is carried out by the 2D non-linear, non-hydrostatic/hydrostatic model NEOWAVE, developed by the UAF and the University of Hawaii (UH). A detailed energy analysis allows us to determine the full development of the tsunami source and the appropriate time of coupling the 3D and 2D models.

Tsunami Source Description

Strong evidence of a submarine landslide is observed in the USGS multibeam bathymetry data of the Mona Passage (ten Brink et al., 2004; Chaytor and ten Brink, 2007) along the northern slope of the Desecheo Ridge, a shallow east-west trending ridge connecting the island of Desecheo with the western tip of Puerto Rico at the location of Punta Higüero in the municipality of Rincón (G#3 in Figure 1). The Desecheo Ridge is an important geologic feature in the Mona Passage because it separates the deepest portions of the Mona Rift leading to the Puerto Rico Trench to the north and the shallow Mayagüez Basin to the south (Chaytor and ten Brink, 2010).

The shallowest portion of the landslide head scarp is located at latitude $18.44°$N and longitude $67.49°$W along the 1320m depth contour. Escarpments are notable at both the left and right sides of the slide allowing a detailed morphology of the landslide to be determined and an area of 76km^2 to be computed (López-Venegas et al., 2008). Seismic reflection profiles covering the landslide domain show the vertical extent of the excavation and portions of the depositional toe of the landslide. Most of the removed material from the landslide may be found dispersed throughout the Mona Rift and further north to the Puerto Rico Trench because the natural downslope in this region reaches deeper than 5000m. As a result, the landslide material is dispersed throughout the Mona Canal down to the Puerto Rico Trench, making it difficult to trace the depositional signature of this event. For a more comprehensive description of the submarine landslide and the methodology to obtain estimates on the volume of material removed by the event, the reader is directed to the publication of López-Venegas et al. (2008).

López-Venegas et al. (2008) concluded that the geometry and orientation of the landslide favors an initial leading depression wave arriving at the western coast of Puerto Rico. Moreover, the combination of distance of the slide with respect to the shore and the bathymetry of the region produces estimates of wave arrivals that are in agreement with the time between the onset of the earthquake and the first observed wave arrival by anecdotal evidence collected by Reid and Taber (1919). These factors are presented as key evidence that supports the landslide as the strongest candidate for the generation of the tsunami. The north slope of the Desecheo Ridge is characterized by a northward, gently dipping carbonate platform featuring numerous faults and cracks. Violent ground shaking produced by the earthquake must have triggered the dislodging of the sediment material along this gently dipping slope, therefore resulting in the generation of the tsunami.

In addition to presenting marine geophysical evidence to justify the landslide as the cause of the tsunami, López-Venegas et al. (2008) also performed tsunami simulations to estimate the landslide velocity and bottom friction coefficient. The tsunami was simulated with COULWAVE (Lynett and Liu, 2002) using a crude rectangular rotational landslide with dimensions obtained from the bathymetry. Although simulations allowed to determine a landslide duration of 325 seconds, and a best-fit bottom friction coefficient ranging from 0.01 to 0.04, the grids employed (1000m and 400m) were too coarse to produce detailed water amplitudes. Finally, limitations of the computational capabilities and the software at the moment were the lack of on-shore inundation and runup computations, an objective this study seeks to accomplish by modeling a more realistic landslide flow with a higher resolution bathymetry.

Description of the Models

For the development of inundation maps of landslide-generated tsunamis, a common approach is to combine a 3D Navier Stokes (NS) model for the landslide-induced waves with a 2D depth integrated non-hydrostatic or Boussinesq model for the wave propagation and runup (coupled model). The 3D NS model determines the wave kinematics and the free surface configuration caused by the landslide (the initial tsunami wave source), which are then input as the initial condition (hot start) to the more numerically efficient 2D non-hydrostatic model for the calculation of the wave propagation and detailed runup.

The 3D NS numerical model, TSUNAMI3D, is based on the Computational Fluid Dynamic (CFD) model develop-

ment originated in Los Alamos National Laboratory (LANL) during the 1970's and follows the early work done by Hirt and Nichols (1981). It solves transient fluid flow with free surface boundaries based on the concept of the fractional Volume of Fluid (VOF) method using an Eulerian mesh of rectangular cells of variable size. The fluid equations solved are the finite difference approximation of the full NS equation and the incompressibility condition equation which results from the continuity equation when the density is constant. The basic mode of operation is for a single fluid phase having multiple free surfaces. However, TSUNAMI3D also can be used for calculations involving two fluid phases separated by a sharp or diffusive interface, for instance, water and landslide material. In either case, both fluids are considered incompressible and treated as Newtonian. Internal obstacles, *e.g.,* topography, wall, etc., are defined by blocking out fully or partially any desired combination of cells in the domain. It is well known that full 3D NS numerical models are highly computationally intensive and require a considerable amount of computer resources. Therefore, TSUNAMI3D has been simplified to overcome as much as possible the computational burden of 3D NS tsunami simulations. The simplification is derived from the large aspect ratio (horizontal/vertical scale) of the tsunami wave and the selected computational cell size required to construct an efficient 3D grid. The large aspect ratio of the tsunami wave requires also a large grid aspect ratio to reduce runtime and memory usage. However, the grid aspect ratio should be smaller than the aspect ratio of the tsunami wave to simplify the fluid surface reconstruction. The standard VOF algorithm, the donor-acceptor technique of Hirt and Nichols (1981), has been simplified to account for this large cell aspect ratio. The pressure term is split into two components, hydrostatic and non-hydrostatic. Although TSUNAMI3D has the capability of variable grids (1D telescoping), it does not comprise the nesting capability (2D telescoping) which is needed for detailed inundation solutions on coastal regions. The interested reader is referred to (Horrillo, 2006; Horrillo et al., 2013) for more detailed information about the 3D NS model.

The 2D depth-integrated and non-hydrostatic model NEOWAVE is built on the non-linear shallow-water equation with a non-hydrostatic pressure term to describe weakly dispersive waves. This approach is equivalent to existing models based on the classical Boussinesq equation. The model features a momentum conserved advection scheme that enables the modeling of breaking waves without the aid of analytical solutions for bore approximation or empirical equations for energy dissipation. An upwind scheme extrapolates the free-surface elevation instead of the flow depth to provide the flux in the momentum and continuity equations. This scheme apparently improves the model stability which is essential for computation of energetic breaking waves and complex runups. The pressure term is split into hydrostatic and non-hydrostatic components, and the vertical velocity is introduced in response to the non-hydrostatic pressure through the three dimensional continuity equation. The interested reader is referred to Yamazaki et al. (2008) to obtain more detailed information about the 2D depth-integrated/non-hydrostatic model.

Both models, TSUNAMI3D and NEOWAVE, have shown very good agreement with the benchmark cases provided by the National Tsunami Hazard Mitigation Program (NTHMP) for tsunami model validation and verification, report OAR-PMEL-135 (Synolakis et al., 2007). Results of the validation and verification of these models can be also found in the NTHMP's Workshop Proceedings (NTHMP, 2012).

3D NS Model's Governing Equations

A schematic of the domain and variables used in TSUNAMI3D is given in Figure 2. The governing equations to describe the flow of two incompressible Newtonian fluids (*e.g.,* water and landslide) are the incompressibility condition of the continuity equation,

$$\frac{\partial u_i}{\partial x_i} = 0, \qquad i = 1, 2, 3 \tag{1}$$

and the nonconservative equation of momentum given by:

$$\frac{\partial u_i}{\partial t} + u_j \frac{\partial u_i}{\partial x_j} = -\frac{1}{\rho_{1,2}} \left(\frac{\partial p}{\partial x_i} + \frac{\partial q}{\partial x_i} \right) + \frac{\partial}{\partial x_j} \left[\frac{\mu_{1,2}}{\rho_{1,2}} \left(\frac{\partial u_i}{\partial x_j} + \frac{\partial u_j}{\partial x_i} \right) \right] + g_i, \qquad i, j = 1, 2, 3 \tag{2}$$

where $\mathbf{u} = [u(x, y, z, t), v(x, y, z, t), w(x, y, z, t)]$ are the velocity components along the coordinate axes $\mathbf{x} = [x, y, z]$ at time t. Here, the given subscripts $1, 2$ indicate physical parameters or variables corresponding to the water and landslide phases, *i.e.,* $\rho_1(x, y, t)$ and $\rho_2(x, y, t)$ are the density of the water and landslide material respectively. The water and landslide phases are considered as Newtonian fluid, therefore, the kinematic viscosity μ_1/ρ_1 and μ_2/ρ_2 can be adjusted for internal friction,, Here μ_1 and μ_2 are the molecular viscosity of the water and landslide material respectively, thus, the landslide friction term in Equation 2 factored by μ_2/ρ_2 can be adjusted according to a constitutive model for landslide rheology, *e.g.,* Bingham model, which is not implemented in this study. The acceleration due to gravity is represented by $\mathbf{g} = [0, 0, -g]$. The total pressure in each phase, $p_{tot} = p + q$, is divided into the hydrostatic pressure p and the dynamic or non-hydrostatic pressure q.

In the water domain the hydrostatic pressure is given by

$$p = \rho_1 g(\eta_1 - z) \tag{3}$$

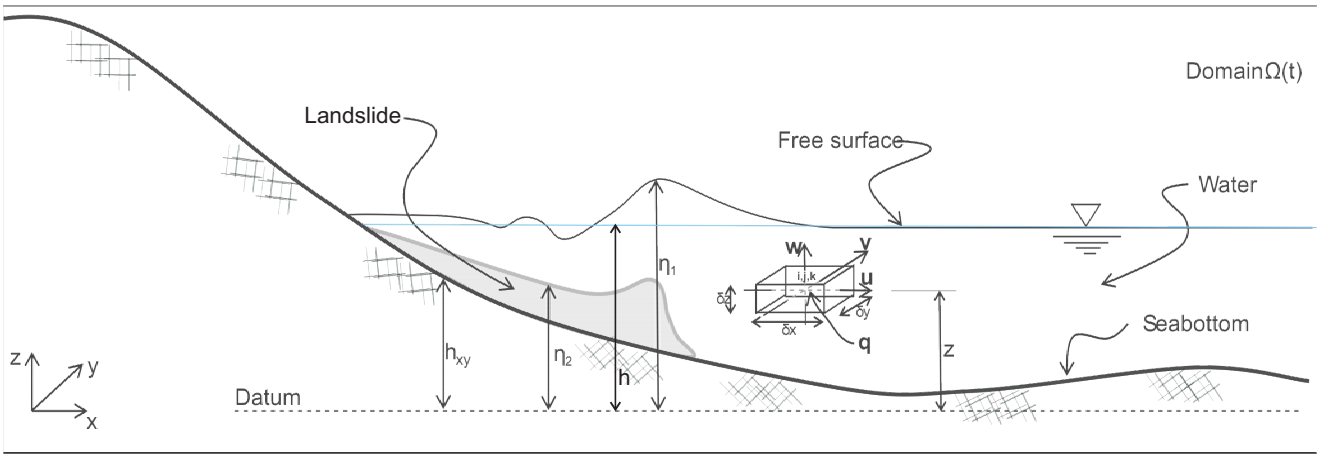

Fig. 2 Sketch of model domain and variables for 3D NS model TSUNAMI3D.

such that $\partial p/\partial z = -\rho_1 g$. Here, z is the elevation measured from the vertical datum to the cell center and η_1 is the water free surface elevation measured from the vertical datum as well.

For the landslide phase, the total pressure $p_{tot} = p + q$, is determined by the hydrostatic pressure as

$$p = g[\rho_1(\eta_1 - \eta_2) + \rho_2(\eta_2 - z)] \tag{4}$$

and the dynamic pressure q. Here η_2 is the landslide free surface elevation measured from the vertical datum. The landslide material is also considered as a Newtonian fluid, with kinematic viscosity, μ_2/ρ_2 for internal friction.

Both water and landslide surface elevations, η_1 and η_2, are traced using the simplified Volume of Fluid (VOF) method based on the scalar function F and the donor-acceptor algorithm of Hirt and Nichols (1981). The method is based on the so-called fraction function F, in which F is defined as the fraction of fluid in the control volume cell (namely, volume of a computational grid cell). F is a discontinuous function, its value varies from 0 to 1 depending of the fluid interface location. Basically, when the cell is empty, with no fluid inside. the value of F is zero; when the cell is full, $F = 1$; therefore, when the fluid's interface is within the cell, then $0 < F < 1$. Details of the simplified VOF method can be also found in Horrillo et al. (2013).

For the discretization of the computational domain, the model uses an Eulerian variable mesh of rectangular cells with large aspect ratio. The governing equations are solved by using the standard explicit finite difference scheme starting with field variables such as $\mathbf{u}$, q and $\eta_{1,2}$ known at time $t = 0$. The governing equations are solved by discretizing the field variables spatially and temporally in the domain to obtain new field variables at any required time. All variables are treated explicitly with the exception of the non-hydrostatic pressure field q, which is implicitly determined (Casulli and Stelling, 1998). Non-linear terms are approximated by using an up-wind down-wind approach up to the third order (Horrillo et al., 2013). The hydrodynamic pressure field q is calculated through the Poisson's equation by using the incomplete Choleski conjugated gradient method to solve the resulting linear system of equations.

The friction term in the momentum equation can be adjusted to mimic the internal friction within the fluid body, *i.e.*, the viscosity coefficient. This coefficient has been chosen to give the best possible agreement with the reference data.

2D Non-hydrostatic Model's Governing Equations

The governing equations for the depth-integrated, non-hydrostatic NEOWAVE model (Yamazaki et al., 2008), are derived from the incompressible Navier-Stokes equation and the incompressibility condition of the continuity equation in a spherical coordinates system in which λ is the longitude, ϕ is the latitude, and z denotes the normal distance from the still water level (SWL). The resulting momentum equations along λ, ϕ, z directions are:

$$\frac{\partial U}{\partial t} + \frac{U}{R\cos\phi}\frac{\partial U}{\partial \lambda} + \frac{V}{R}\frac{\partial U}{\partial \phi} - \left(2\Omega + \frac{U}{R\cos\phi}\right)V\sin\phi = -\frac{g}{R\cos\phi}\frac{\partial \zeta}{\partial \lambda} - \frac{1}{2}\frac{1}{R\cos\phi}\frac{\partial Q}{\partial \lambda} - \frac{1}{2}\frac{Q}{DR\cos\phi}\frac{\partial(\zeta - h_b + \eta_{co})}{\partial \lambda} - n^2\frac{g}{D^{1/3}}\frac{U\sqrt{U^2+V^2}}{D} \tag{5}$$

$$\frac{\partial V}{\partial t} + \frac{U}{R\cos\phi}\frac{\partial V}{\partial \lambda} + \frac{V}{R}\frac{\partial V}{\partial \phi} + \left(2\Omega + \frac{U}{R\cos\phi}\right)U\sin\phi = -\frac{g}{R}\frac{\partial \zeta}{\partial \phi} - \frac{1}{2}\frac{1}{R}\frac{\partial Q}{\partial \phi} - \frac{1}{2}\frac{Q}{DR}\frac{\partial(\zeta - h_b + \eta_{co})}{\partial \phi} - n^2\frac{g}{D^{1/3}}\frac{V\sqrt{U^2+V^2}}{D} \tag{6}$$

$$\frac{\partial W}{\partial t} = \frac{Q}{D} \tag{7}$$

and the continuity equation reads

$$\frac{\partial(\zeta-\eta_{co})}{\partial t}+\frac{1}{R\cos\phi}\frac{\partial(UD)}{\partial\lambda}+\frac{1}{R\cos\phi}\frac{\partial(VD\cos\phi)}{\partial\phi}=0 \tag{8}$$

where U, V and W are depth-averaged velocity components in the λ, ϕ and z directions respectively. The variable t is the time, ζ is the free surface elevation from the SWL, R is the earth's radius, Ω is the earth's angular velocity, ρ is the water density, Q is the non-hydrostatic pressure, g is the gravitational acceleration and n is the Manning's coefficient for the sea-bottom friction. The vertical velocity W is assumed to have a linear distribution along the water column, therefore the vertical velocity component W is simply the average value of the vertical velocity at the free surface and the seafloor. The total depth is defined as $D=\zeta+(h_b-\eta_{co})$, where h_b is the water depth (from SWL to seafloor) and η_{co} is the seafloor co-seismic deformation (η_{co} is not considered in this study). A detailed discussion of NEOWAVE numerical scheme, solution and capability is found in Yamazaki et al. (2008).

3D-2D Coupling Process

One critical step in the coupling process of the two models is to determine the right moment of transferring the 3D model's wave and water kinematic (u,v and w) and free surface (η_1) field to the 2D non-hydrostatic model. The right time of transferring is controlled by the 3D domain size, and the total energy on the water induced by the submarine landslide. The 3D domain must be large enough to fully develop the generated waves without leaving the domain boundaries, and the wave energy should reach a maximum indicating that the generated waves are fully or mostly developed. If the domain size-energy considerations have been fulfilled, then the 3D field information or variables (u,v,w and η_1) are converted to two dimensions by a simple column-wise depth averaging and inputted as the initial condition (hot start) to the 2D non-hydrostatic numerical model.

Energy Equations

The generated waves are determined to have been fully developed when the total (potential plus kinetic) wave energy reaches a maximum. Energy in the system (3D domain) is determined at each phase (water and landslide) from the equations of classical mechanics by integrating each control volume or computational cell energy over the entire domain. The potential energy of the deformed water surface is measured in terms of η_1-h, the free surface elevation from the SWL (see Figure 2). The wave's potential energy per unit horizontal area is given by

$$E_{P_{Water}}=\frac{1}{2}\rho_1 g(\eta_1-h)^2. \tag{9}$$

The water or wave's kinetic energy is a function of the square of the velocity:

$$E_{K_{Water}}=\frac{1}{2}m_1(u^2+v^2+w^2) \tag{10}$$

where m_1 is the mass of the water fraction (F) in the control volume.

The energy of the landslide material can be calculated in a similar manner. The potential energy of the landslide material is measured in terms of the submerged sediment density $\rho_2-\rho_1$ and the distance of the landslide surface η_2 from the vertical datum. The landslide potential energy per unit horizontal area is then given by

$$E_{P_{Slide}}=\frac{1}{2}(\rho_2-\rho_1)g(\eta_2-h_{xy})(h_{xy}+\eta_2) \tag{11}$$

where h_{xy} is the height of the seafloor from the vertical datum (see Figure 2 for reference). The landslide kinetic energy equation is again similar to that of the water:

$$E_{K_{Slide}}=\frac{1}{2}m_2(u^2+v^2+w^2) \tag{12}$$

with m_2 the mass of the fraction (F) of the landslide material in the control volume. Assuming a still water condition at $t=0$, all energies are zero except for the potential energy of the landslide ($E_{P_{Slide}}(0)$), which has a value based on the landslide's location with respect to the reference vertical datum. At any time t, the change in landslide potential energy $E_{P_{Slide}}(0)-E_{P_{Slide}}(t)$ gives the amount of energy released into the system at that time.

Similar energy analysis was performed by Abadie et al. (2012) using a 2D numerical model for a landslide tsunami and by Sue et al. (2006) using a block slide experimental setup. Abadie et al. (2012) calculated potential and kinetic energy of the water/wave ahead of the landslide by integrating the energies from the tip of the landslide to the boundary of the computational domain. Sue et al. (2006) used data measurements to calculate potential and kinetic energy of the block landslide as well as the potential energy of the resulting wave, thereby relating the energy of the landslide to the energy transferred to the wave. Here, we are able to perform a more comprehensive 3D energy analysis as the potential and kinetic energy of the wave and landslide can be easily calculated separately in time by integrating the respective energies from each computational cell, depending on the cell's fractional amount of water and/or landslide material. This allows a more complete view of the complex energy behavior in landslide motion, tsunamigenesis, and physical/numerical losses.

Results: 3D Landslide-Tsunami Simulation

The model TSUNAMI3D was used to perform the full-scale 3D numerical simulation to calculate the initial tsunami wave based on our assumption that the earthquake triggered an underwater landslide. The resulting mass wasting of the Mona tsunami underwater landslide is approximately 155m thick (in average), $\sim$ 10.5km long, $\sim$ 7.7km wide and slides (initially) over a slope of $\sim$ 10%. The wasting volume of $\sim$ 12.5km^3 used in this numerical simulation is larger than the one reported in López-Venegas et al. (2008) and ten Brink et al. (2006) of 10.0km^3. The discrepancy is attributed to the different slide dimension obtained by following more precisely the scarp borders and probably by the different method used for the calculation of the volume. The landslide volume reported herein was calculated by projecting tangentially the existing immediate isobath located at the undisturbed edges of the scarp to create smooth surfaces between the projected isobath, gridding these smooth surfaces, and subtracting these surfaces from the gridded bathymetry of the scarp. On the other hand, the landslide volume reported by López-Venegas et al. (2008) and ten Brink et al. (2006) was calculated by interpolating smooth surfaces through polygons that define the edges of the slide.

Figure 1 shows the bathymetry of the Puerto Rico's northwest corner that surrounds the Mona scarp. The shadowed region on Figure 1 indicates the 3D domain used by the TSUNAMI3D model. The 3D domain dimension box is 0.6 arc-degree (east-west) $\times$ 0.5 arc-degree (south-north) and 5.10km high. The south-north horizontal dimension of the domain is approximately 55.6km long, and at latitude of $\sim$ 18.55 N arc-degrees, the east-west horizontal dimension is approximately 63.26km long. The domain grid resolution is $720\times600\times337$ cells in the x, y and z direction, respectively, for a total of 145.6 million cells. Thus, the model's horizontal spatial steps are 87.86×92.67m (x,y) and the vertical spatial step is variable ranging from 1m to 8m. The finer vertical resolution was confined in the water free surface and water-landslide interface regions, in contrast with the coarser vertical resolution which was confined in the deeper water regions. The time step size is variable with a minimum value of 0.05 sec. The seawater and landslide densities have assigned values of 1025kg/m^3 and 2000kg/m^3, respectively. A Newtonian fluid approach has been assumed for the water-landslide system; the viscosity coefficients (kinematic viscosity) μ_1/ρ_1 and μ_2/ρ_2 have been set to 1×10^{-6}m^2/sec as a conservative assumption to obtain greater landslide downslope acceleration, tsunami wave amplitude and runup. The free slip condition is applied in all fluid cells neighboring a seabottom cell, *i.e*, $\partial\mathbf{u}/\partial z=0$. At an early state of a full-scale landslide downslope movement, a Newtonian fluid assumption for the landslide material is reasonable valid if one seeks a conservative initial tsunami wave. It is also true that a Newtonian fluid will not come to rest completely. However, as the initial tsunami wave characteristic is mainly controlled by the early landslide kinematics and slide characteristics (initial slide acceleration, size, slope, sediment properties, etc.) and not by the subsequent slide evolution in deeper water. As the landslide reaches deeper water, the effects of the landslide kinematics only cause minor changes to the main tsunami characteristics (Haugen et al., 2005; Grilli and Watts, 2005; Watts et al., 2005). It is also observed that massive landslides have longer runout distances. Basal-friction and shear-rate seem to reduce as the landslide thickness/volume increases. The larger the slide volume, the greater the thickness and the smaller the shear rate (Campbell et al., 1995). Therefore, assuming no basal friction at the initial state of the wave generation or even assuming an almost inviscid flow for the landslide-water system is a valid and conservative supposition for a full-scale event. The geological footprint in deeper water of many large fan systems originated by ancient submarine landslides supports this simplified assumption of a Newtonian fluid for the landslide material.

Computer time required to simulate 10 minutes of the Mona Passage underwater landslide and tsunami was $\sim$ 48 hours using a cluster with 32 CPUs assigned. The 3D simulation results of the landslide-induced tsunami waves are shown in Figure 3. Left panels of Figure 3 show snapshots of the evolution of the underwater landslide at 0.5, 1.5 and 3 minutes, and the respective evolution of the free surface is shown on panels to the right. As can be observed from Figure 3 (use the color bar as a reference), a wave of $\sim$ 48m high (crest to trough) is recorded after 3 minutes of the slide initiation. The outgoing positive wave with amplitude of $\sim$ 18m is followed by a backgoing negative wave or initial surface depression of $\sim$ 30m caused by the fast downslope motion of the underwater landslide. Notice that a rebounding wave is emerging from the surface depression between the outgoing and the negative backgoing wave (panels (b) and (c)). The rebounding wave does not evolve as a massive wave as the outgoing wave, but as a short and highly dispersive wave.

The energy produced by the landslide and resulting tsunami wave is presented in Figure 4. Panel (a) shows the change of potential energy and the kinetic energy of the landslide. The change of the landslide potential energy is presented as the difference from the initial potential energy and the potential energy at time t, $E_P(0)-E_P(t)$. This difference accounts for the produced energy that is released at time t into the system after the landslide motion begins (t=0). The landslide kinetic energy initially increases and then begins to level off after $\sim$ 160 sec. As mentioned above, the assumption of a Newtonian fluid means the landslide material will not come to a complete rest, therefore the produced energy continues to increase, but the landslide stops accelerating after less than 3 min. As found by Sue et al. (2006), the initial change of potential energy of the landslide is converted mostly into

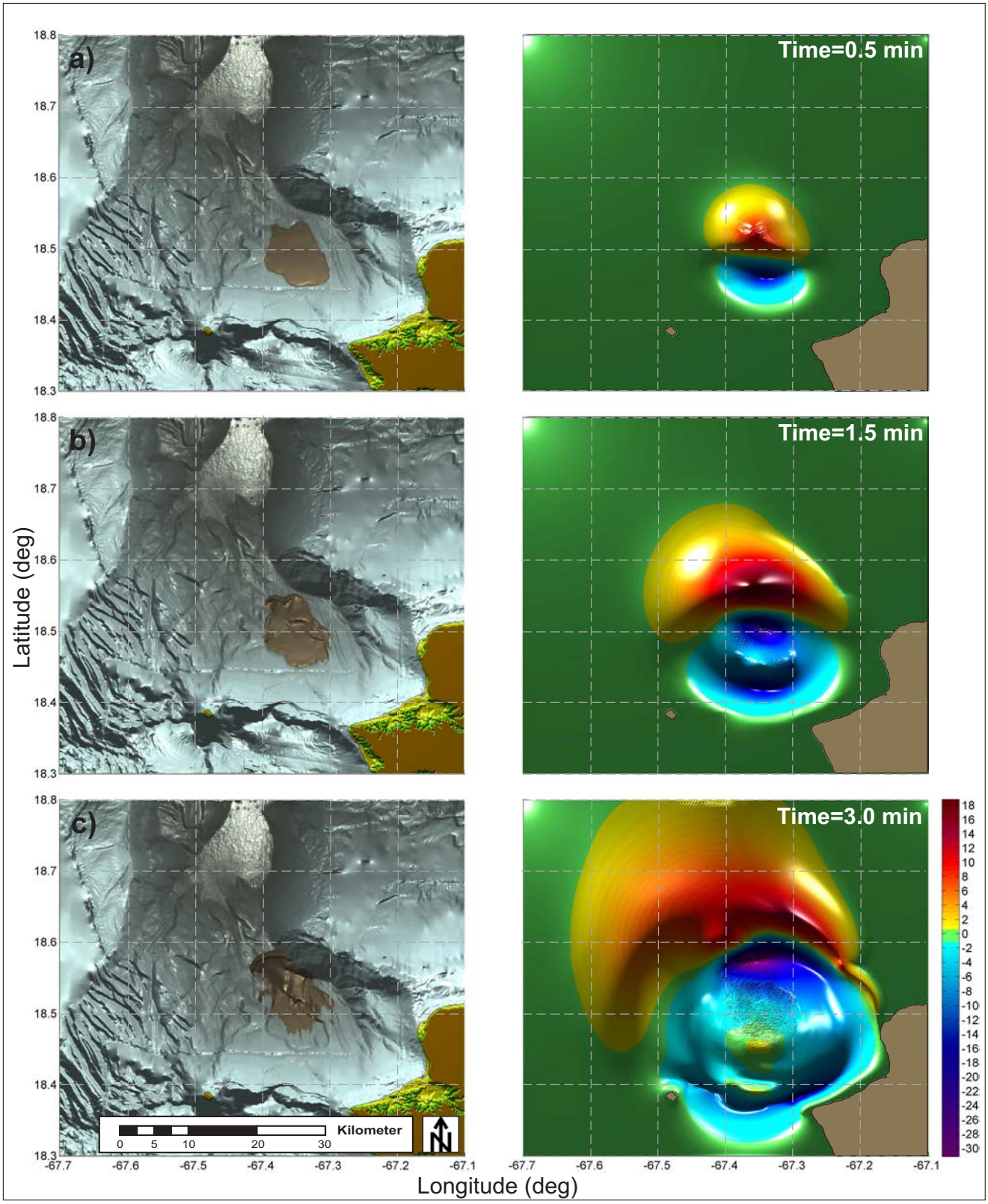

Fig. 3 TSUNAMI3D results: submarine landslide evolution (left column) and tsunami wave evolution (right column) at times 0.5 (top row), 1.5 (mid row) and 3 minutes (bottom row). Colorbar in meters

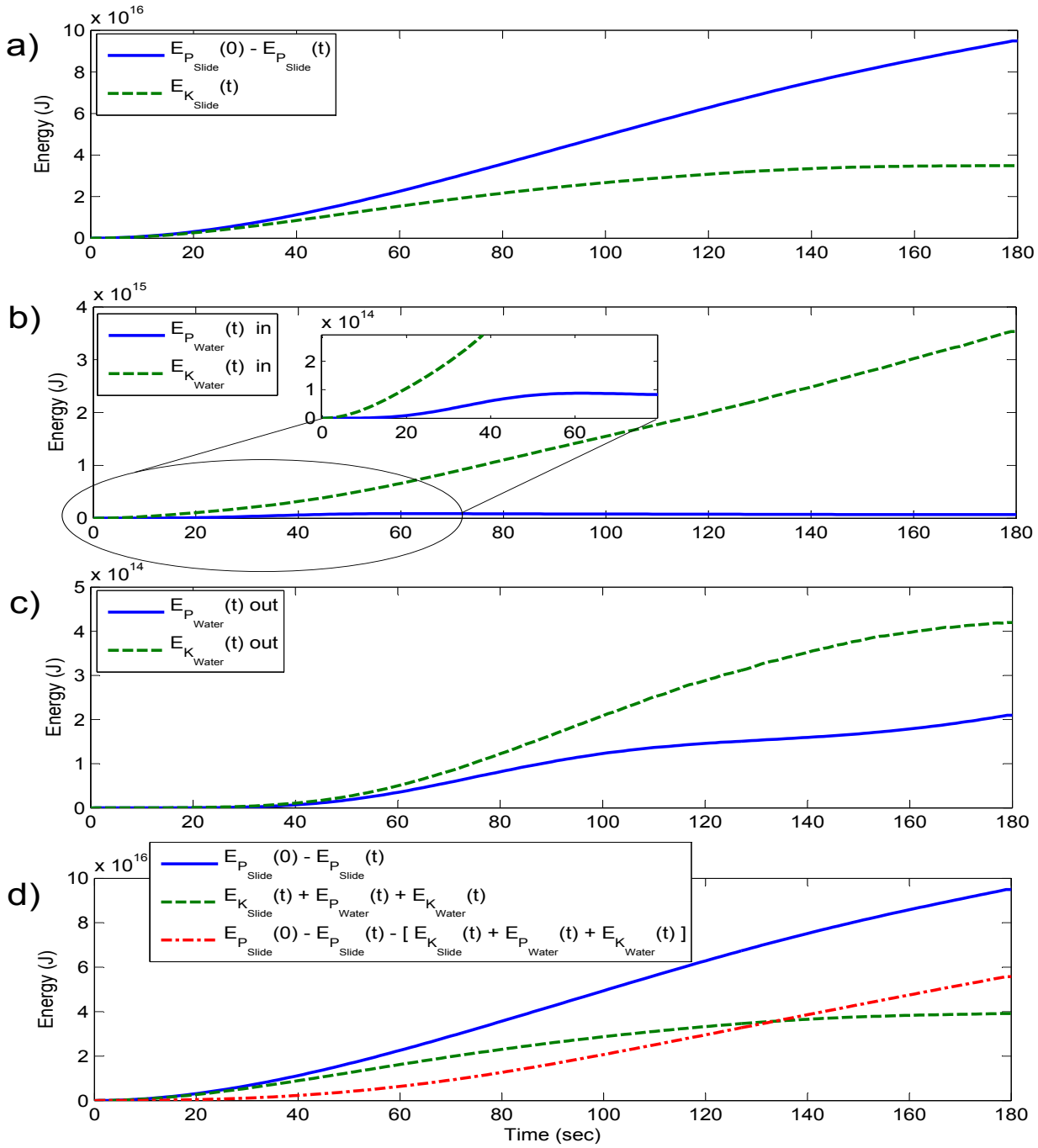

Fig. 4 Potential-released and kinetic energy of the landslide and resulting wave inside and outside the wave generation area. Panel (a), potential energy released by the landslide (solid line) and kinetic energy of the landslide (dashed line). Panel (b), potential (solid) and kinetic (dashed) energy of the water inside the generation area. Panel (c), potential (solid) and kinetic (dashed) energy of the water outside the generation area. Panel (d), energy budget comparison between the potential energy released by the landslide and the total energy transfered into the system (landslide kinetic + water kinetic + water potential).

landslide kinetic energy as the landslide begins moving, i.e., $t < 40\ sec$. This kinetic energy is then transferred into kinetic energy of the water as the moving landslide sets the water around it into motion. The water movement deforms the free surface, converting some of the water kinetic energy into potential wave energy. For example, at early state (< 20 sec) after the onset of the landslide, the potential energy given off by the landslide is mostly converted to land-

slide kinetic energy. Also during this time a small fraction of the landslide potential energy inside the generation area starts to be converted to water kinetic energy and wave potential energy (Figure 4 Panel (b)) with values of one and two order of magnitude smaller.

We partition the water energy based on the location of the landslide to account for the energy that propagates away from the wave generation area separately from the energy inside the generation area, see also Abadie et al. (2012). The outgoing and backgoing propagating waves, which are those that propagate outside of the generation area, are of principal interest for tsunami inundation and hazard assessment. Also, we determine the development of the tsunami wave in terms of the energy released in the system based on the energy budget outside the generation area and thus the appropriate time to transfer the wave information from the 3D model (TSUNAMI3D) to the 2D model (NEOWAVE). The generation area is defined in time by flagging computational cells horizontally surrounding the landslide; here, we mask 4 cells on any side of a cell which contains landslide material at any point in time, resulting in a 9×9 horizontal grid surrounding any landslide cell. Inside the generation area, the kinetic water energy is summed on water cells column-wise from the surface of the landslide to the free water surface, and outside the generation area this kinetic energy is summed on water cells column-wise from the seafloor to the free water surface.

Panel (b) of Figure 4 shows the potential and kinetic energy of the water inside the generation area; likewise, panel (c) shows the water energy outside the generation area. Clearly, we see that the water kinetic energy is largely affected by the landslide motion, as the kinetic energy of the water in the generation area continues to increase substantially with the continued landslide motion and is approximately one order of magnitude larger than the kinetic energy outside the generation area (compare dashed lines in panels (b) and (c)). However, inside the generation area the potential water energy is almost two orders of magnitude less than the kinetic energy and reaches a maximum early on (after ~ 62 sec, see the zoomup on panel (b)) as the initial wave begins to leave the generation region. Outside the generation area, panel (c), the wave potential energy is about twice as large as that inside the generation area due to the large amplitude of the initial tsunami waves and to the subcritical regime (Froude number $F_r = V_s/\sqrt{gD} < 1$, where V_s is the average landslide velocity, D the total water depth, and g the gravity acceleration) for this specific underwater landslide. The potential and kinetic energy of the water outside the generation region level off or reach a maximum by 180 sec (3 minutes) approximately. Effectively, once the initial large wave propagates away from the generation region, its energy stabilizes. While Abadie et al. (2012) found that the equipartition of wave energy away from the landslide was very nearly half potential and half kinetic, the kinetic energy determined here is approximately twice as large as the potential energy; this difference is most likely because equipartition of energy may not hold immediately during the generation process of the wave, see Fritz et al. (2004) and Watts (2000). The large difference might be enhanced by the inclusion of the third spatial dimension in contrast to the $2D$ model in Abadie et al. (2012). Equipartition of water energy outside the generation area is expected to occur later on in the wave propagation process.

As a result of these energy calculations, we conclude that the majority of energy transfer from landslide to wave occurs in the first few minutes of wave generation, as also found by Abadie et al. (2012). Potential energy conversion into water energy of this 3D deep-submerged landslide ranges between 3.5% to 4.5%, magnitude comparable to other submerged landslide studies, e.g., Watts (2000) (3%-7%, with respect to the landslide kinetic energy) and Sue et al. (2006) (1.1%-5.9%, with respect to the landslide potential energy). While significant wave energy within the generation region continues, the increasing depth of the landslide limits any further tsunamigenic potential after the initial wave is formed. Therefore, the tsunami wave is mostly developed by the time it reaches the boundary of the computational domain and 3 minutes is an appropriate time to transfer the wave information from TSUNAMI3D to NEOWAVE for the detailed inundation calculation.

Figure 4, panel (d) gives a comparison of the total energies. The solid line shows the total energy input into the system by the landslide potential energy and the dashed-dotted line represents the energy loss. In a closed system, the potential energy released by the landslide would be converted completely into landslide kinetic energy plus total water/wave energy (dashed line). However, there is a considerable difference between these energies in our model result. This is a topic of continued study, but we believe this is largely due to numerical diffusion which is expected to be more substantial in a 3D numerical model. Nevertheless, we still are able to include small additional friction through the viscosity coefficient while keeping basal friction negligible, meaning that "physical friction" is kept at a minimum. In more realistic or complex model settings, for example, in a domain with complicated bathymetry as we have here, we are aware that numerical models undergo substantial numerical diffusion or energy dissipation in regions where waves shoal or runup. The numerical diffusion effect is well observed when waves travel over a sloping seabottom, see Kowalik (2008), as the nonlinear terms are usually reduced to an upstream/downstream numerical form. For example, in a 1D $x-$direction scheme, the numerical diffusion associated to the first order of approximation (positive ve-

locity) for the nonlinear term reads

$$\frac{u_p h_x}{2}\frac{\partial^2 u}{\partial x^2} \tag{13}$$

where u_p is the resulting water or slide downstream particle velocity from the upstream/downstream numerical scheme, and h_x is the space step or the $x-$direction grid resolution. This term (Equation 13) is similar to the friction term in the momentum equation (Equation 2) with viscosity coefficient (artificial-numerical viscosity $u_p h_x/2$) being a function of the space step h_x and the downstream particle velocity u_p. The artificial-numerical viscosity coefficient is large in shallow water regions where wave particle velocities are larger, enhanced further by the shoaling or slope gradient. On the other hand, in deeper water with a uniform or smooth seabottom bathymetry, particle wave velocities (i.e., u_p) are very small and the numerical diffusion caused by the nonlinear terms is small too. In these regions, the numerical diffusion takes place in the short wave length range, being determined by how well short waves are resolved by the spatial step. Waves generated by submarine/subaerial landslides are very dispersive and are degraded quickly in multiple short waves; therefore, the model's numerical scheme will quickly dissipate these short waves that are in or close to the unresolved scale ($2h_x$), see Kowalik (2008).

Additionally, a depth-profile of the wave kinetic energy density in J m^{-3} within the wave generation area is shown in Figure 5. This seems to be an interesting analysis of the energy behavior within the water column and allows a further understanding of the water dynamics associated with the landslide. The kinetic energy density of the wave is largely concentrated near the landslide, which reaches from a depth of approximately -1200 to -3000m initially, and -1200 to -3500m after 3 minutes. The depth interval of main energy concentration grows with time, so that the energy imposed by the landslide reaches higher into the water column, but it is mainly concentrated deeper than -1200m. There is a small amount of energy density at the surface associated with the free surface motion, but it is minimal compared to the maximum at greater depth. At the beginning, the energy density maximum occurs just above the leading edge of the landslide. This maximum may also be amplified at later times (after $\sim$ 120 sec) by a rebounding of landslide material from the face of a cliff in the seafloor. A secondary maximum occurs over the middle part of the landslide at earlier times (before around 60 sec), then becomes increasingly pronounced above a deepening portion of the leading edge. Interestingly, at 152 sec, the energy densities above the shallower and deeper portions of the leading edge are nearly balanced, and thereafter the maximum energy density shifts to the deeper portion, with the energy near the shallower part becoming a secondary maximum as the leading edge smoothes and flattens. At 3 minutes, when the wave information is transferred to the 2D model, a maximum energy density of 8.2×10^4 J m^{-3} is calculated at -3052m depth.

Table 1 Numerical Gauge location

Gauge number*	Station Name	Longitude ($^\circ W$)	Latitude ($^\circ N$)	Water Depth(m)
G#1	Old Lighthouse (Punta Borinquen)	67.162423	18.494596	13.0
G#2	Aguadilla	67.161112	18.429514	36.0
G#3	Rincón Lighthouse (Punta Higüero)	67.274675	18.364380	15.0

* See Figure 1

By using the numerical code NEOWAVE with the nested grids shown in Figure 1, detailed tsunami runup was obtained in present-day Aguadilla, *i.e.*, sealevel elevation (runup), water depth (inundation) and maximum momentum flux quatities. Figure 6 shows the tsunami inundation results in Aguadilla calculated on the innermost grid ($1/3$ arc-second resolution) of the nested grid domain. Panel (a) in Figure 6 portraits the maximum runup or sealevel elevation with reference to the Mean High Water (MHW) level. Panel (b) on the same figure shows the inundation depth defined as $D = \zeta - h$; where ζ is the sealevel elevation and h is the land elevation with respect to the MHW level. It is important to mention that regions with inundation depth shallower than 1ft (~ 0.30m) are not indicated in the figure. Numerical results show that the overall maximum water elevation in the populated area of present-day Aguadilla ranges from 3 to 9m. Consequently, the maximum inundation depth ranges from 0.30 - ~ 6.0m.

Three nearshore numerical gauges have been located in the domain to record the profile in time of the tsunami waves as they approach Puerto Rico's western coastal region (see Figure 1). Table 1 shows the location of the numerical gauges, and their results are depicted in Figure 7. According to Reid and Taber's survey, all locations in western Puerto Rico experienced a tsunami leading depression wave. In the Old Lighthouse (Punta Borinquen - G#1), the lighthouse keeper observed the sea receding shortly after he felt the main shock, while the Rincón lighthouse keeper at Punta Higüero (G#3) witnessed that the sea returned $\sim$ 2 minutes after it receded shortly after the earthquake. Several important observations can be derived from the numerical simulation results. The initial wave to approach the shore was indeed a negative wave, and this negative wave reached the coastline facing Aguadilla about 5 minutes after the landslide initiation (see G#2 wave profile, middle panel on Figure 7). This is consistent with the arrival time observations presented by Reid and Taber (1919) and the computations presented by both Mercado and McCann (1998) using a dislocative source, and López-Venegas et al. (2008), using a submarine landslide source.

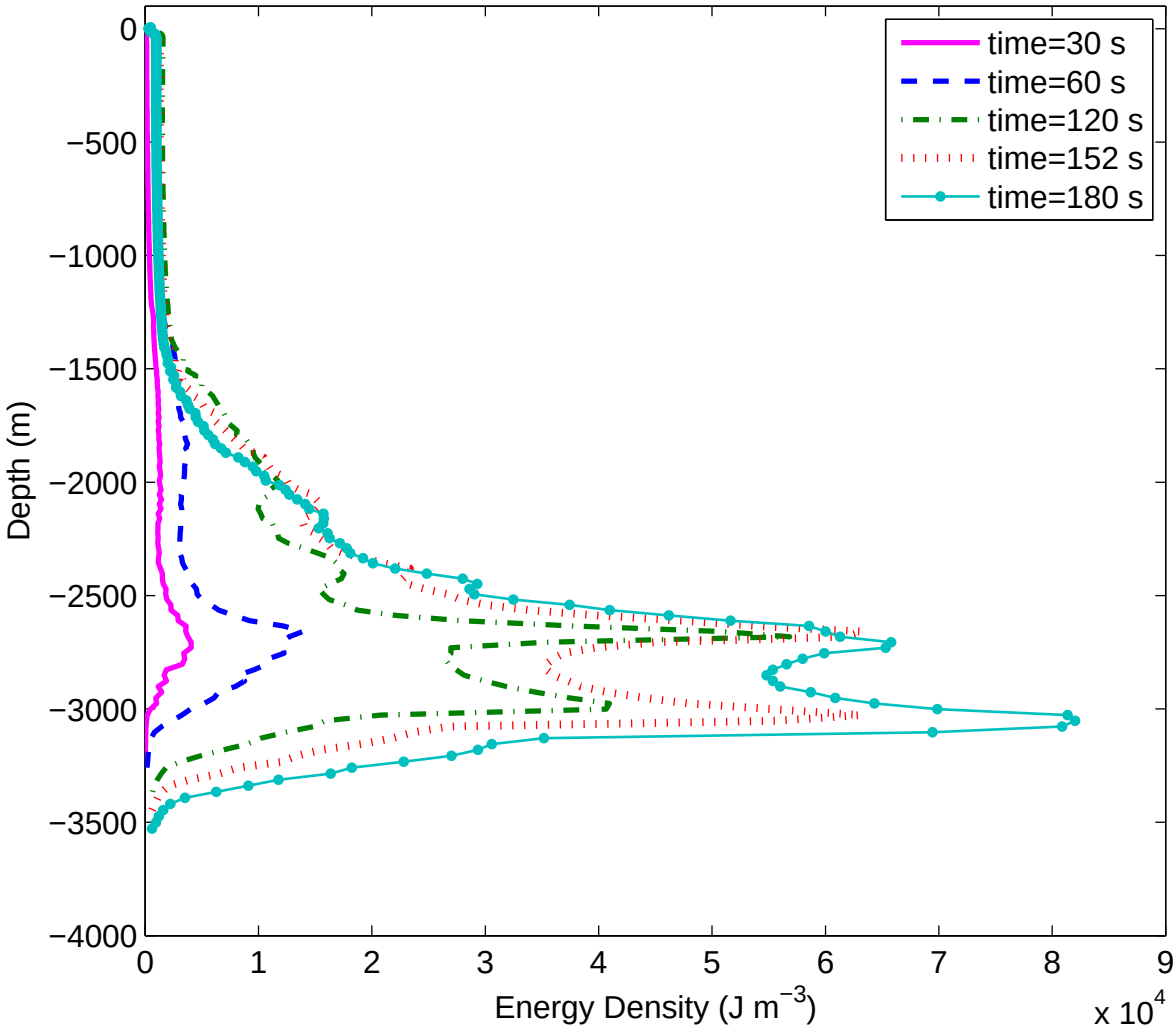

Fig. 5 Depth profile of water kinetic energy density within generation area at selected times during wave generation.

Our simulations yield a maximum wave amplitude of 2.2m at 13m depth offshore the coast at Punta Borinquen (upper panel on Figure 7), with on-shore runup of 4.8 to $\sim$ 5.4m (see color scale inside upper red triangle that is indicating the location of the Old Lighthouse on panel (a) of Figure 6). The runup model result is slightly higher than the estimated 4.6m on-shore runup value from the post-tsunami survey, but considerably lower than the 8.3m obtained from the previous modeling study of López-Venegas et al. (2008). At the numerical gauge offshore of Aguadilla (G#2) (middle panel on Figure 7), the model's maximum wave amplitude of the approaching wave is estimated at 4.2m at a depth of 36m, and the runup in the area of the old downtown (lower red triangle on Figure 6, panel (a)) ranges from 4.8m to 7.2m. These values are in agreement with the $>$ 4.0m values estimated by the survey and still significantly lower than the 12.8m estimated by López-Venegas et al. (2008). The extent of flooding in Aguadilla is accurately predicted by the model, which flooded partially the town square located West of San Carlos Borromeo Church, two blocks east of the beachfront (Figure 8). Witnesses indicate that the tsunami penetrated up to the town square but not to the Church. Finally, for the third numerical gauge (G#3) at Punta Hig¨uero, which is located at a depth of 15 m, wave maximum amplitude is estimated to be 7.1m. Surprisingly, the positive wave came shortly after the negative wave, as it was witnessed by the Rincón lighthouse keeper (see lower panel on Figure 7). Unfortunately, this location is outside the 1/3 arc-second grid, thus detailed runup was not computed; however, higher values for runup were obtained on-shore that were not in agreement to either the survey of Reid and Taber (1919) (5.5m) or the results of López-Venegas et al. (2008) (5.9m).

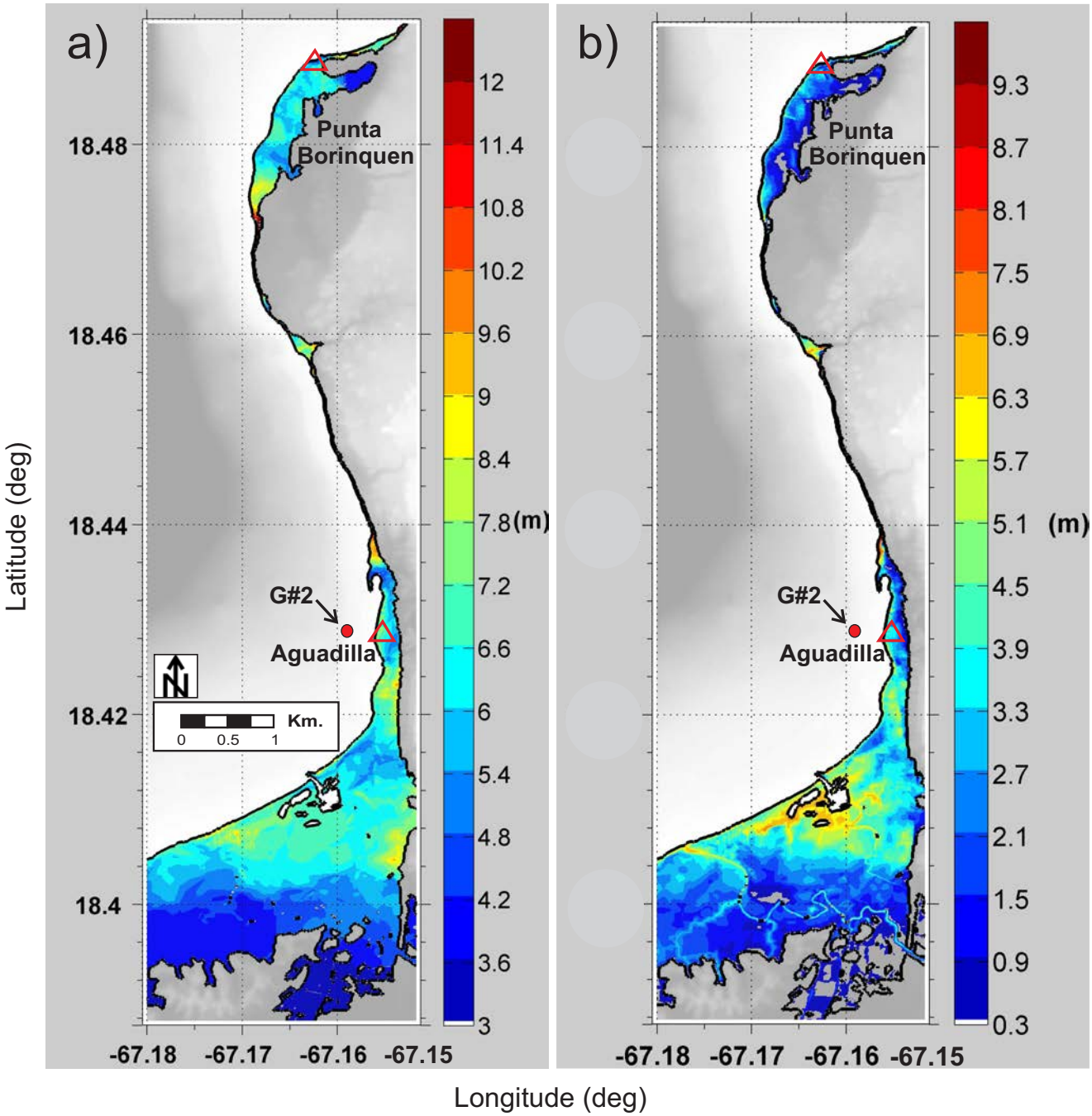

Fig. 6 Numerical results in Aguadilla calculated on the innermost grid ($1/3$ arc-second resolution) of the nested domain. Panel *(a)*, maximum runup or sealevel elevation. Panel *(b)*, maximum inundation depth.

In this particular region, the topography features coastal cliff and shallow water. Therefore, a nested grid with increasing resolution should be considered in future research to estimate precisely the runup and inundation extent nearby the Rincón lighthouse at Punta Higüero.

Our results are in better agreement to the values obtained from the post-tsunami survey of Reid and Taber (1919) than those obtained from the previous numerical model of López-Venegas et al. (2008). Therefore, we conclude that simulations at both G#1 and G#2 fit well the observations, whereas the simulation might slightly overestimate at G#3. These values are corroborated by the NEOWAVE inundation simulation in Figure 6. The fact that slightly higher values are obtained is related to the internal friction of the landslide, which here is kept to a minimum for estimating potential damage for the present-day coast if a similar event were to happen today.

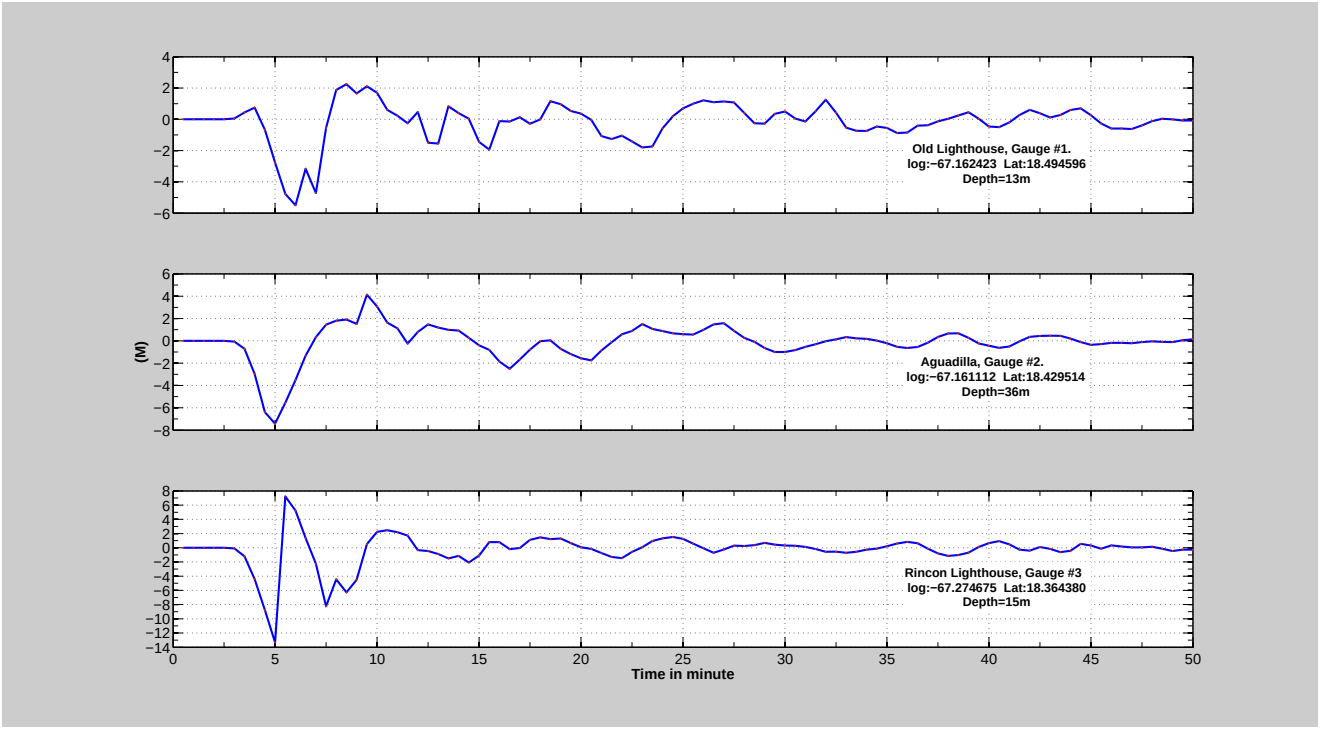

Fig. 7 Numerical gauges results at three different locations indicated in Table 1 and previously surveyed by Reid and Taber (1919). Upper panel (G#1), Old Lighthouse at Punta Borinque; middle panel (G#2), Aguadilla; lower panel (G#3), Rinc´on Lighthouse at Punta Higüero. See Figure 1 for geographic location of gauges.

Although the landslide main motion is directed toward the north, a fraction of the tsunami energy is refracted around Puerto Rico's northwest shelf, hence producing waves that impact Puerto Rico's north coastline. A separate study is underway to quantify these effects, as these waves would be highly dispersive for a landslide source, therefore allowing to help discriminate among the postulated sources.

The tsunami momentum flux quatities was also calculated to determine potential for inland damage from the flow forces. The momentum flux quantities could be useful for engineering design purpose or re-assessment of existing structures, or assisting coastal managers in assessing the relative vulnerability of some infrastructure or in identifying the nature and location of major tsunami flows. Figure 9 shows the magnitude of the inundation depth and water flow velocity at maximum momentum flux. The inundation depth shown in panel (a) of Figure 9 corresponds to the inundation depth at the time when the maximum momentum flux occurs. It is important to mention that this inundation depth is slightly different from the maximum inundation depth portrayed in panel (b) on Figure 6. In the same manner, the flow velocity, shown in Figure 9 panel (b), corresponds to the velocity when the maximum momentum flux takes place. These quantities are valuable for the determination of flow forces on some sensitive structures along the tsunami runup path.

Assuming a steady flow, the inundation forces exerted on a surface-piercing structure can be evaluated with the following hydrodynamic force equation,

$$F = \frac{1}{2}\rho C_d (b \times h) u^2 \tag{14}$$

where ρ is the fluid density; C_d is the drag coefficient; and $b \times h$ is the wetted area of the body projected on the plane normal to the flow direction, (Yeh, 2007). The fluid force at a given location can be determined by Equation 14 using the combined values of hu^2 (momentum flux quantity) shown in Figure 9 panel (c). A complete discussion of tsunami forces acting on structures can be found in Yeh (2007). From Figure 8 it can be gleaned that the water entering the city is stopped by the road embankment structure which acts as an inundation protection system. Overall, the momentum flux quantity in the populated area of Aguadilla ranges from 25 to 125 m$\times$(m/sec)^2 per unit mass and per unit breadth.

These quantities can be useful to estimate the flow forces on a structure according to its location in the inundation area. For example, in 1893, a monument to commemorate the 400^{th} anniversary of Christopher Columbus landing in Puerto Rico was erected south of the former mouth of the Culebrinas River, the boundary between the town of Aguadilla ($\sim$ 2km due northeast) and Aguada. The "Cross of Columbus", also called the "Columbus Monument", consists of a ~ 10m^3 base supporting a pillar of ~ 2.4m^3 plus a stack of several granite blocks of square sections forming a column (~ 2.35m^3) which supports the capstone cross (~ 0.75m^3).

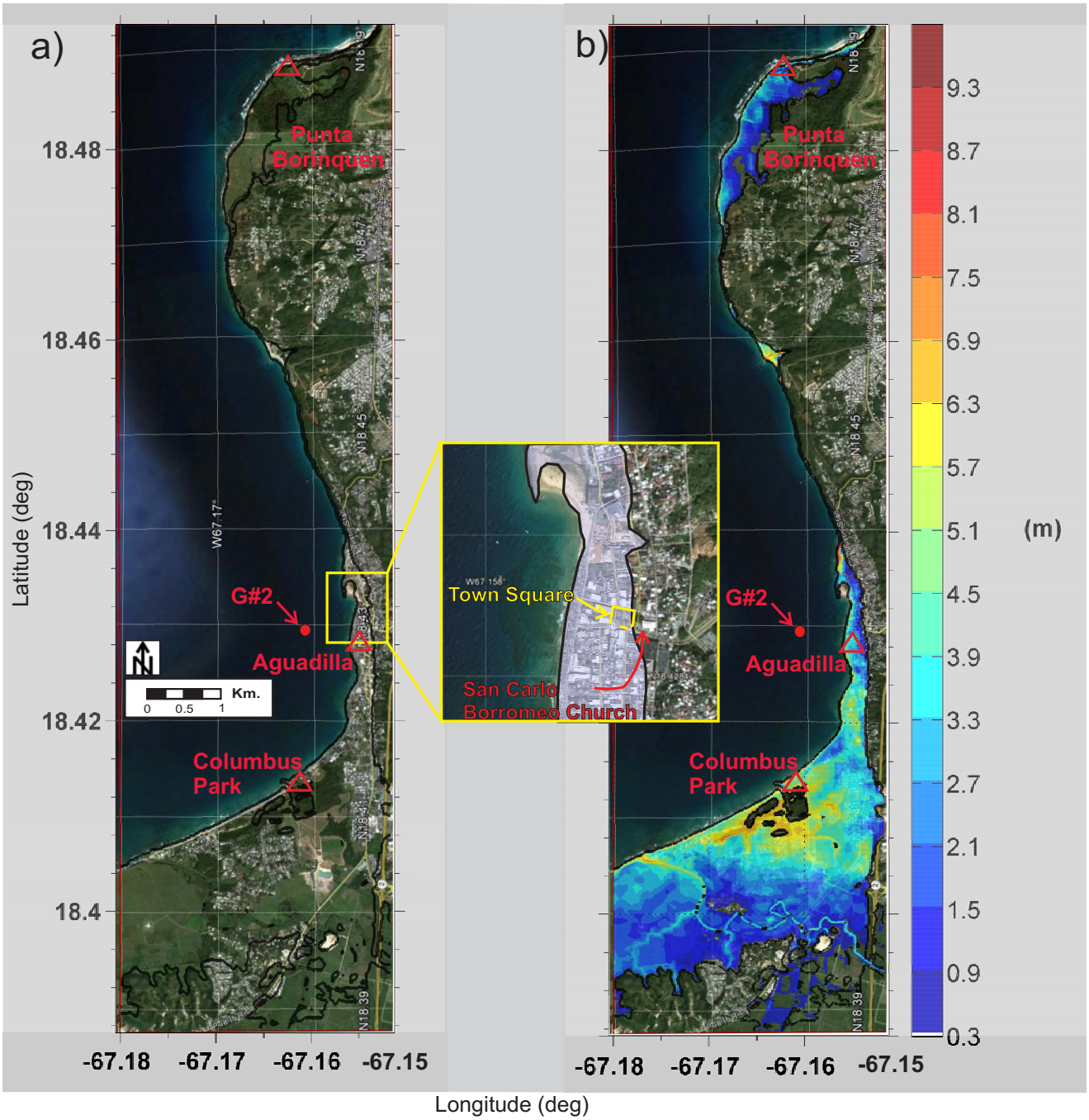

Fig. 8 Tsunami inundation extent in present-day Aguadilla (northwest Puerto Rico) assuming the hypothetical case of the Mona tsunami of October 11, 1918. Panel *(a)*, the inundation limits map, and panel *(b)*, inundation depth map, are placed side by side to facilitate visualization of the inundation level with respect to the populated areas. Plan view is taken from GoogleEarth ©.

The total height of the monument may have reached up to 10m and may have stood up to 100m from the shore. According to Reid and Taber (1919), the monument, except for its massive base, collapsed during the earthquake, and in turn, tsunami waves carried the monument blocks to distances between 45 and 75m landward. In 1923, an exact replica of the monument was built using the original base, therefore helping in the assessment of tsunami forces that may have affected the piercing structure during the tsunami. By means of the information obtained from Figure 9, it is possible to do a rough estimation of the force and overturning moment that may have affected the pillar of the Columbus monument under the tsunami load, where $h = 3.9$m and $u = 8.1$m/s are obtained from the color scale at Columbus Park (lower triangle on Figure 9). The assessment is performed by assuming that the pillar survived the earthquake

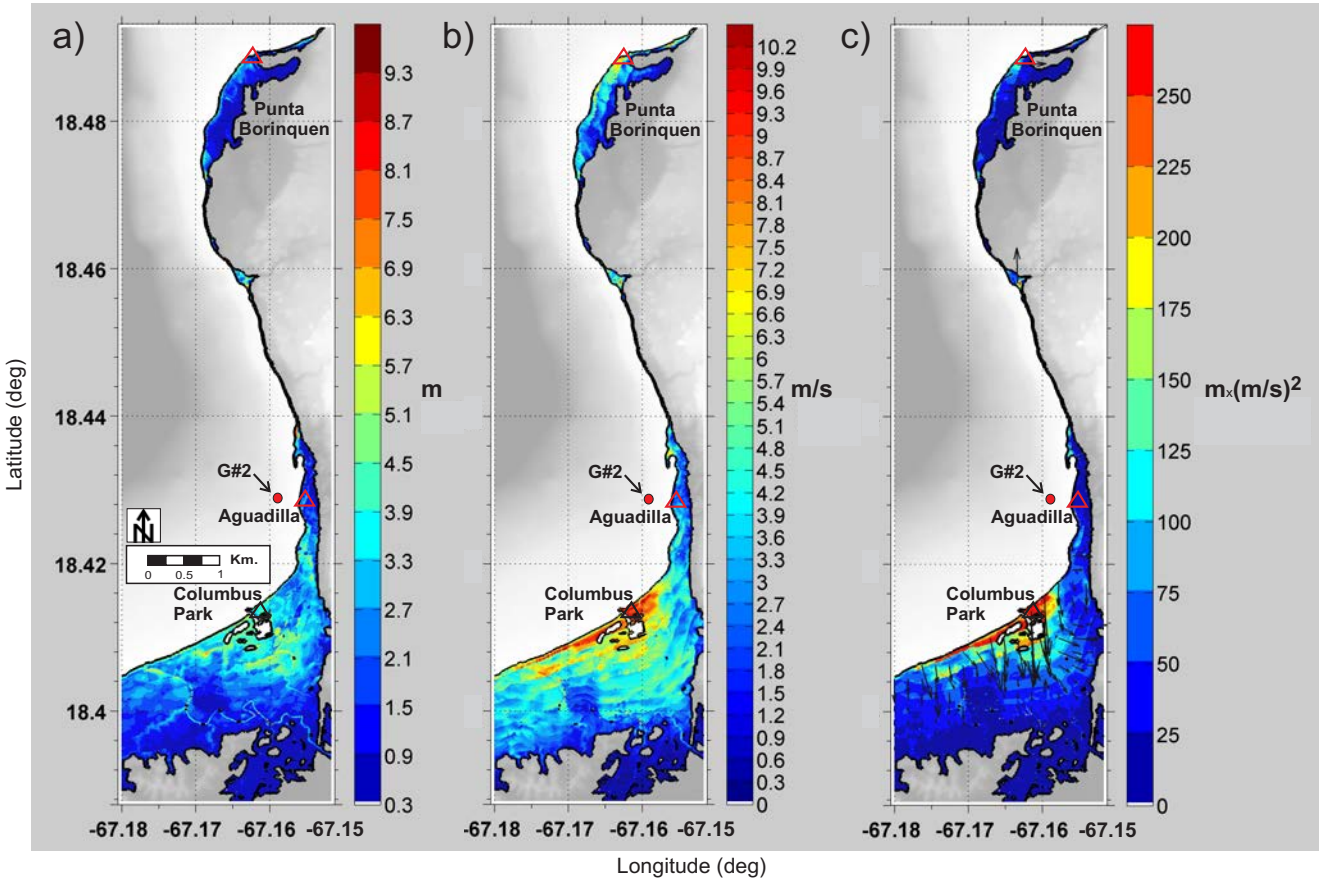

Fig. 9 Numerical results in Aguadilla computed on the innermost grid ($1/3$ arc-second resolution) of the nested grid domain. Panel *(a)*, inundation depth at maximum momentum flux. Panel *(b)*, water velocity at maximum momentum flux. Panel *(c)*, maximum momentum flux quantity.

and was destroyed later by the tsunami flow load. The pillar has a cross section of $\sim 1.2 \times 1.2\text{m}^2$ and stands up on the base at 1.2m above the ground, therefore the pillar has an effective flow height of $h = 3.9 - 1.2 = 2.7$m. Now, by considering a steady flow at the maximum momentum flux in view of the fact that tsunamis have a long period, Equation 14 can be applied. Following the work of Yeh (2007), a drag coefficient of 2 ($C_d = 2$) was used in the calculation. At the base of the piercing structure we thus obtain a shear force of ~ 213kN and an overturning moment of $\sim 288\text{kN}\times\text{m}$. The restoring moment owned to the weight of the granite monument ($\rho_{granite} = 2750\text{kg/m}^3$) partially submerged during the tsunami load is $\sim 115\text{kN}\times\text{m}$ which is much less than the overturning moment.

Conclusions

This study presents an improved numerical simulation for the October 11, 1918 tsunami observed along the northwestern coast of Puerto Rico. The work and simulations presented here are based on the assumption that this tsunami was generated by a massive submarine landslide triggered by the earthquake. This study builds on previous research of this event by employing an advanced computational system for submarine landslides, in which a well-established and validated 3D/2D coupled model is presented and applied, yielding results comparable to observations. For the 3D phase the Navier-Stokes model TSUNAMI3D for two fluids (water and landslide material) was used to determine the initial wave characteristic generated by the submarine landslide. To solve for coastal inundation, *i.e.*, wave propagation and detailed runup, the 2D non-hydrostatic numerical model NEOWAVE was used. The 3D model provides the wave kinematic and the free surface configuration for the initial tsunami wave source, which were then input as the initial condition (hot start) to the more numerically efficient 2D model.

The full-scale 3D numerical simulation used a wasting volume of $\sim 12.5\text{km}^3$ to generate the initial tsunami wave. A wave of ~ 48m high (crest to trough) was recorded after 3 minutes of the slide initiation. The outgoing northward positive wave with amplitude of ~ 18m was followed by a landward negative wave or initial surface depression of ~ 30m. Shortly, a rebounding wave emerged from the surface depression between the outgoing and negative backgoing waves, though this rebounding wave did not evolve as a

massive wave, but as a short and dispersive wave. The negative wave reached the coastline facing Aguadilla in about 5 minutes after the landslide initiation. These estimates are consistent with the observations of a leading depression and arrival times collected from witnesses. Although the landslide main motion is directed toward the north, a fraction of the tsunami energy is refracted around the Puerto Rico's northwest shelf, apparently impacting the north coastline. A subsequent publication will address this question and the impact along the northern coast of Puerto Rico.

Analysis of the potential and kinetic energy of the system showed that the energy of the wave is largely affected by the landslide motion in the generation region, and this energy is mainly concentrated within the wave generation area and at depth near the surface of the landslide. Once the initial wave begins to propagate away from the generation area, its potential and kinetic energy begin to stabilize. Since the energy outside the generation area is what is propagated toward shore and is therefore of importance for inundation and hazard studies, the stabilization of the wave energy in this region indicates the appropriate time to transfer the wave kinematic and free surface information from the full 3D model to the 2D model for detailed inundation calculation.

By using two-way nested grids of 1 and $1/3$ arc-second with the 2D numerical code NEOWAVE, detailed tsunami runup was obtained in Aguadilla, *i.e.*, sealevel elevation (runup), water depth (inundation) and maximum momentum flux quantities. Figure 8 shows the tsunami inundation extent in present-day Aguadilla, assuming a hypothetical tsunami case that the Mona landslide event were to occur today. The expected maximum water elevation in the populated area of Aguadilla ranges from 3 to 9m with maximum inundation depth from 0.30 - ~ 6.0m respectively.

Numerical calculation showed that the water entering the city is stopped by the road embankment structure that acts as an inundation protection system. The momentum flux quantity in the populated area of Aguadilla ranges from 25 to $125\text{m}\times(\text{m/sec})^2$ per unit mass and per unit breadth. The momentum flux values are important for engineering design purposes or re-assessment of existing structures to verify their capability to resist tsunami loads. In addition, this parameter can assist coastal managers in assessing the relative vulnerability of some infrastructure by identifying the nature and location of major tsunami flows.

Acknowledgments

This study was funded through the National Tsunami Hazards and Mitigation Program (NTHMP) awarded to the Puerto Rico Seismic Network tsunami component. Numerical calibration of the 3D numerical model was in part supported by the National Science Foundation (NSF) through the NSF-NEESR award CMMI-0936603. The authors wish to thank the valuable help from Harry Justiniano and Jos´e Benítez from the Physical Oceanography Laboratory at the Marine Sciences Department - UPRM, and IT staff from PRSN. All wishes to thank Uri ten Brink and Jason Chaytor from the Woods Hole Science Center, USGS. Special thanks go to the reviewers for their comments and suggestions, which significantly contributed to improving the quality of this paper.

References

Abadie, S.D., Morichon, S.D., Grilli, S., Glockner, S., 2008. VOF/Navier-Stokes numerical modeling of surface waves generated by subaerial landslides. La Houille Blanche, 1, 21–26.

Abadie, S.D., Morichon, S.D., Grilli, S., Glockner, S., 2010. Numerical simulation of waves generated by landslides using a multiple-fluid Navier-Stokes model. Coastal Engineering, 57, 779–794.

Abadie, S.M., Harris, J.C., Grilli, S.T., Fabre, R., 2012. Numerical modeling of tsunami waves generated by the flank collapse of the Cumbre Vieja Volcano (La Palma, Canary Islands): Tsunami source and near field effects. J. Geophys. Res. 117, C05030.

ten Brink, U., Danforth, W., Polloni, C., Andrews, B., Llanes, P., Smith, S., Parker, E., Uozumi, T., 2004. New seafloor map of the Puerto Rico Trench helps assess earthquake and tsunami hazards. Eos Trans. AGU, 85, 349,354.

ten Brink, U., Dillon, W., Frankel, A., Rodríguez, R., Mueller, C., 1999. Seismic and tsunami hazard in Puerto Rico and the Virgin Islands. Open-File Report 99-353. U.S. Geological Survey.

ten Brink, U.S., Geist, E., Andrews, B.D., 2006. Size distribution of submarine landslides and its implication to tsunami hazard in Puerto Rico. Geoph. Res. Lett. 33, 4.

Campbell, C.S., Cleary, P.W., Hopkins, M., 1995. Large-scale landslide simulations: Global deformation, velocities and basal friction. J. Geophys. Res. 100(B5), 8267-8283.

Casulli, V., Stelling, G.S., 1998. Numerical simulation of 3D quasihydrostatic, free-surface flows. J. Hydr. Eng. 124, 678–686.

Chaytor, J., ten Brink, U.S., 2007. Two-stage Extensional Opening of the Mona Passage as Revealed by New Multibeam Bathymetry and Seismic Reflection Data. Eos Trans. AGU, 88(52), Fall Meeting Suppl., Abstract T13C–1475.

Chaytor, J., ten Brink, U.S., 2010. Extension in Mona Passage, Northeast Caribbean. Tectonophysics, 493, 74–92.

Doser, D.I., Rodríguez, C.M., Flores, C., 2005. Historical earthquakes of the Puerto Rico-Virgin Islands region (1915-1963), in: Mann, P. (Ed.), Active tectonics and seismic hazards of Puerto Rico, the Virgin Islands, and off-

shore areas. The Geological Society of America. Special Paper 385, pp. 103–114.

Dunbar, P.K., Weaver, C.S., 2008. U.S. States and Territories National Tsunami Hazard Assessment: Historic Record and Sources for Waves. Technical Report Report to National Tsunami Hazard Mitigation Program. NGDC, USGS.

Fritz, H., Hager, W.H., Minor, H.E., 2004. Near field characteristic of landslide generated impulsive waves. J. Wtrwy. Port Coast. and Oc. Eng. ASCE 130 (6), 287–302, doi:10.1061/(ASCE)0733-950X(2004) 130:6(287).

Grilli, S.T., Watts, P., 2005. Tsunami generation by submarine mass failure part I: modeling, experimental validation, and sensitivity analyses. J. Wtrwy. Port Coast. and Oc. Eng. ASCE 131 (6), 283–297.

Haugen, K.B., Lovholt, F., Harbitz, C.B., 2005. Fundamental mechanisms for tsunami generation by submarine mass flows in idealized geometries. Mar. Pet. Geol. 22, 209–217.

Hirt, C.W., Nichols, B.D., 1981. Volume of fluid method for the dynamics of free boundaries. J. Comp. Phys. 39, 201–225.

Hornbach, M.J., Mondziel, S.A., Grindlay N.R., Frohlich C., Mann P., 2008. Did a submarine slide trigger the 1918 Puerto Rico tsunami? Science of Tsunami Hazards, 27, No.2, 22-31.

Horrillo, J., 2006. Numerical Method for Tsunami calculations using Full Navier-Stokes equations and the Volume of Fluid method. Ph.D. thesis. University of Fairbanks.

Horrillo, J., Wood A., Kim, G.-B, A. Parambath A., 2013. A simplified 3-D Navier-Stokes numerical model for landslide-tsunami: Application to the Gulf of Mexico. J. Geophys. Res. Oceans, 118, 6934-6950, doi:10.1002/2012JC008689.

López-Venegas, A.M., ten Brink, U.S., Geist, E., 2008. Submarine landslide as the source for the October 11,1918 Mona Passage tsunami: Observations and modeling. Marine Geology, 254, 35–46.

Kowalik, Z., 2008. Energy flux as a tool in locating tsunami secondary sources. Science of Tsunami Hazards, 27, No.3, 1–29.

Lynett, P., Liu, P.L., 2002. A numerical study of submarine landslide generated waves and runup. Proc. Royal Society of London A. 458, 2885–2910.

Mercado, A., McCann, W., 1998. Numerical simulation of the 1918 Puerto Rico tsunami. Natural Hazards, 18, 57–76.

NTHMP, 2012. National Tsunami Hazard Mitigation Program, in: Proceedings and Results of the 2011 NTHMP Model Benchmarking Workshop; NOAA Special Report, Boulder: U.S. Department of Commerce/NOAA/NTHMP. p. 436.

Reid, H.F., Taber, S., 1919. The Porto Rico earthquakes of October-November, 1918. Bull. Seismol. Soc. Am. 9, 95–127.

Sue, L. P., Nokes, R. I., Walters, R. A., 2006. Experimental modeling of tsunami generated by underwater landslides. Science of Tsunami Hazards, 24, No.4, 267–287.

Synolakis, C.E., Bernard, E.N., Titov, V.V., Kanoglu, U., Gonzalez, F.I., 2007. OAR PMEL-135 Standards, criteria, and procedures for NOAA evaluation of tsunami numerical models. Technical Report NOAA Tech. Memo. OAR PMEL-135. NOAA/Pacific Marine Environmental Laboratory, Seattle, WA.

Watts, P., 2000. Tsunami features of solid block underwater lanslide. J. Waterw. Port Coast. Ocean Eng. 126 (3), 144–152.

Watts, P., Grilli, S.T., Tappin, D.R., Fryer, G.J., 2005. Tsunami generation by submarine mass failure. part II: Predictive equations and case studies. J. Waterw. Port Coast. Ocean Eng. 131 (6), 298–310.

Yamazaki, Y., Kowalik, Z., Cheung, K.F., 2008. Depth-integrated, non-hydrostatic model for wave breaking and run-up. Int. J. Numer. Meth. Fluids, 61 (5), 473–497.

Yeh, H., 2007. Design tsunami forces for onshore structures. Journal of Disaster Research, 2, No.6.